Imaging with Therapeutic Acoustic Wavelets – Short Pulses Enable Acoustic Localisation when Time of Arrival is Combined with Delay and Sum

Harry J. Davies†, *Member, IEEE,* Sophie V. Morse†, *Member, IEEE,* Matthew J. Copping, Krit Sujarittam, Victor D. Bourgin, Meng-Xing Tang, *Senior Member, IEEE* and James J. Choi*

***Abstract* — Passive acoustic mapping (PAM) is an algorithm that reconstructs the location of acoustic sources using an array of receivers. This technique can monitor therapeutic ultrasound procedures to confirm the spatial distribution and amount of microbubble activity induced. Current PAM algorithms have an excellent lateral resolution, but have a poor axial resolution, making it difficult to distinguish acoustic sources within the ultrasound beams. With recent studies demonstrating that short-length and low-pressure pulses – acoustic wavelets – have therapeutic function, we hypothesized that the axial resolution could be improved with a quasi-pulse-echo approach and that the resolution improvement would depend on the wavelet's pulse length. This paper describes an algorithm that resolves acoustic sources axially using time of flight and laterally using delay-and-sum beamforming, which we named axial temporal position passive acoustic mapping (ATP-PAM). The algorithm accommodates a rapid short pulse (RaSP) sequence that can safely deliver drugs across the blood-brain barrier. We developed our algorithm with simulations (k-wave) and in vitro experiments for 1-, 2-, and 5-cycle pulses, comparing our resolution against that of two current PAM algorithms. We then tested ATP-PAM in vivo and evaluated whether the reconstructed acoustic sources mapped to drug delivery within the brain. In simulations and in vitro, ATP-PAM had an improved resolution for all pulse lengths tested. In vivo, experiments in mice indicated that ATP-PAM could be used to target and monitor drug delivery into the brain. With acoustic wavelets and time of flight, ATP-PAM can locate acoustic sources with a vastly improved spatial resolution.**

***Index Terms* — therapeutic ultrasound, acoustic cavitation, passive cavitation detection, passive acoustic mapping.**

Manuscript received March 31, 2020; revised xx xx, 2020; accepted xx xx, 2020. Date of on-line publication xx xx, 2020; date of current version xx xx, 2020. This work was supported by Alzheimer's Research UK (ARUK-IRG2017A-7). *Asterisk indicates corresponding author*.

H. J. Davies was with the Department of Bioengineering, Imperial College London, SW7 2AZ London, U.K. He is currently with the Department of Electrical and Electronic Engineering, Imperial College London, SW7 2AZ, London, U.K. (e-mail:harry.davies14@imperial.ac.uk).

S. V. Morse (email: sophie.morse11@imperial.ac.uk), M. J. Copping (email: m/copping16@imperial.ac.uk), K. Sujarittam (e-mail: krit.sujarittam17@imperial.ac.uk), M. X. Tang (e-mail: mengxing.tang@imperial.ac.uk) and J. J. Choi* (e-mail: j.choi@imperial.ac.uk) are with the Department of Bioengineering, Imperial College London, SW7 2AZ London, U.K.

V. D. Bourgin was with the Department of Bioengineering, Imperial College London, SW7 2AZ London, U.K. He is currently with the Department of Bioengineering, University of Cambridge, CB2 1PZ, Cambridge, U.K (email: vb406@cam.ac.uk).

†These authors contributed equally to this work.

I. Introduction

ULTRASOUND technologies in conjunction with microbubbles can non-invasively and locally treat tissue. In these techniques, microbubbles are systemically administered into the bloodstream and driven by ultrasound into volumetric expansions and contractions. The microbubble activity exerts mechanical forces onto its surrounding, producing biological responses such as drug delivery across the blood-brain barrier (BBB) [1], drug release from capsules [2] and dissolution of blood clots [3]. Despite the promise of non-invasive treatments, conventional feed-forward therapeutic ultrasound methods remain unpredictable and can potentially produce side effects, such as haemorrhage or cell damage. Without a suitable monitoring and feedback system, therapeutic ultrasound techniques will likely remain uncontrollable.

A promising area of research in therapeutic ultrasound is the delivery of drugs across the BBB. The BBB provides a homeostatic molecular environment for the central nervous system by regulating the transport of molecules to and from the bloodstream [4], [5]. Cerebral capillaries restrict the passage of most molecules above 400-500 Da [6], [7], which means that most useful drug classes – peptides, antibodies, nanoparticles, etc. – cannot be delivered to the brain [6]–[10]. As a result, drugs have continued to fail in clinical trials for brain cancers, Alzheimer's disease and other neurological diseases; and many more drugs have not even entered clinical trials, because they had little hope for success. Therapeutic ultrasound has the potential to reverse this trend by delivering drugs across the blood-brain barrier [11]. Yet, despite significant progress over the last several years, concerns remain with the consistency, distribution and safety of the drug delivery process. For example, in mouse studies, histological analysis of brain regions within the ultrasound beam revealed both areas where drugs were delivered without any detectable damage and areas where drugs were delivered along with red blood cells [12]–[14], indicating potential haemorrhage. A possible explanation for the different safety and performance outcomes within the same ultrasound beam may be that different types of microbubble activity are being generated within the beam.

The microbubbles used are typically small, gas-filled bubbles with a polymer or lipid shell that can be injected into the bloodstream [15]. Ultrasound can non-invasively stimulate the bubbles, because it can travel through tissue. Focused ultrasound drives cavitation of the microbubbles, which produces a mechanical force in the local capillary microenvironment [16]. However, different types of

microbubble activity can be generated by different bubbles, due to several variations. First, microbubble sizes, shell properties and gas contents may vary from bubble to bubble. Thus, different bubbles respond differently to a given excitation. Second, the exact acoustic pressure that each microbubble is exposed to is unknown. There are inter-individual variabilities of acoustic properties of soft tissue, which attenuate and distort the ultrasound to different degrees. For transcranial applications, variations in the skull thickness and microstructure also greatly influence the degree of this pulse distortion.

A microbubble subjected to the compressional pressure phase of an ultrasound pulse will contract before expanding in the accompanying rarefactional phase [17]. At low peak-rarefactional pressures, the microbubble may oscillate between two states of contraction and expansion and is referred to as non-inertial cavitation. When the rarefactional pressure is sufficiently high, the microbubble will expand rapidly and collapse violently, potentially disrupting its surrounding environment. This is known as inertial cavitation [18]. Both cavitation modes can deliver drugs across the BBB, however, high magnitudes of inertial cavitation have been associated with tissue damage in specific contexts [19], [20]. Non-inertial cavitation or low magnitude inertial cavitation provide a safer and more effective method of delivery to the brain [21]–[23]. Due to the contrasting bioeffects of the different types and magnitudes of cavitation and the inability to predict cavitation in an in vivo setting, methods are needed to non-invasively identify and resolve cavitation activity.

Passive acoustic mapping (PAM) is a method that locates acoustic sources by processing the source's acoustic emissions that have been captured with an array of receivers. Two main PAM algorithms are currently used in laboratory experiments: time exposure acoustics (TEA) and the Robust Capon Beamformer (RCB). Time exposure acoustics passive acoustic mapping (TEA-PAM) has been able to recreate acoustic maps in both in vitro and in vivo experiments [24]–[26]. It has also been used to map cavitation activity to drug release from liposomes and to the delivery of adenoviruses [27]. Despite this, TEA-PAM displays significant artefacts, such as crosses and long tail streaks, making it difficult to resolve closely located acoustic sources within the ultrasound beam. Robust capon beamformer passive acoustic mapping (RCB-PAM) decorrelates noise, which improves the resolution of TEA-PAM [25], [28]–[30]. The algorithm assigns different weights to each array element so that noise and interference are minimized [30], [31]. The weights also adapt to specific data and address calibration errors in the equipment. RCB-PAM has been shown to reduce artefacts arising in TEA-PAM and improves the axial resolution [25]. RCB removes between 40% and 50% of tail artefacts, whilst preserving greater than 90% of the energy estimated by TEA-PAM [25]. Other attempts to limit artefacts involve delay and sum beamforming specific to cavitation frequency bands [32], [33], and further extension on the principles of RCB with the use of higher order statistics [34]. There have also been attempts to reduce the computational demands of RCB in order to improve real-time frame rates [35], [36]. However, despite many of these algorithms showing improvements in resolution, they cannot resolve cavitation events within an ultrasound beam in vivo at clinically relevant microbubble concentrations.

An algorithm known as power cavitation imaging, using a short pulse of ultrasound for therapy, has recently been published which incorporated absolute time delays and delay-and-sum beamforming to improve the axial resolution of PAM [37]. The algorithm used a short pulse emitted in a sequence that has not yet been thoroughly evaluated for safety and efficacy; and the emitter and receivers were placed at arbitrary angles from each other. Furthermore, although calculating the power of cavitation with improved resolution was demonstrated, the source strength term was not derived, which is useful to describe the temporal features of the acoustic source at a particular location.

Conventionally, targeted BBB opening has been accomplished using long pulse lengths of approximately 1 ms to 30 ms [11], [12], [27], [38], [39]. BBB disruption has also been demonstrated using shorter pulse lengths (2.3-10 μs); a scale factor of approximately four orders of magnitude less than used previously [40]–[45]. These short pulses have achieved more uniform drug delivery patterns compared to the ms-long pulses, although the drug doses delivered were low or high pressures were required. More recently, a rapid short-pulse sequence (RaSP) has been developed to promote microbubble stimuli that safely delivers molecules while suppressing stimuli that damage tissue [46]–[48]. This RaSP sequence improved the efficacy and safety of drug delivery to the brain in vivo and has inspired the development of the axial temporal position (ATP)-PAM imaging algorithm presented in this paper.

Here, we describe an imaging algorithm that uses therapeutic acoustic wavelets (i.e., short-duration, low-pressure pulses). This algorithm incorporates time-of-flight calculations and delay-and-sum beamforming to simultaneously improve the imaging axial resolution and remove imaging artefacts associated with other passive methods. The use of short wavelets allowed a similar imaging method to plane wave imaging [49]–[51] to be performed directly with the therapeutic pulse, i.e. without introducing additional imaging pulses. We have also defined the source strength, which is essential to characterizing the temporal and spectral features of the cavitation activity. After describing the algorithm in depth, we will explain how we validated the algorithm using three methods: simulations utilizing the k-wave MATLAB toolbox [52], in vitro experiments involving the sonication of microbubbles within two thin tubes, and in vivo experiments which aimed to deliver drugs across the BBB while simultaneously mapping the acoustic energy generated by the microbubbles. Our algorithm was implemented with axially aligned transducers and receivers while using therapeutic acoustic wavelets in a RaSP sequence.

II. Materials and Methods

A. Passive acoustic mapping algorithms

In this section, we describe two existing PAM algorithms – TEA-PAM and RCB-PAM – and then our algorithm ATP-PAM. In all three methods, the purpose is to create a map of acoustic sources in space by capturing and processing their acoustic emissions, using an array of receivers.

1) Time Exposure Acoustics (TEA)

Time Exposure Acoustics attempts to locate acoustic sources without knowing when the sound is generated, which is similar to receive beamforming using delay and sum in conventional pulse echo ultrasound. The algorithm attempts to reconstruct the sound produced at a selected point **r** (i.e., a pixel or voxel) using acoustic emissions captured with a receiver array. A spatial map of acoustic sources (i.e., a 2-D or 3-D image) is constructed by repeating this procedure for every point in the desired field of view.

Sound generated at a point **r** can be reconstructed by assuming that acoustic sources radiate sound spherically. With this assumption, the distance between a point **r** and a sensor array element $\mathbf{r_i}$ is predictable and can be measured by the expected time of flight. This time delay is then applied to all channels, which aligns the signals that have been emitted from the point of interest. The signals are then averaged and the signals originating at point **r** will add up coherently while other signals will be incoherent and thereby suppressed. This strengthens the acoustic signal from **r** relative to signals from other locations.

Thus, with a sufficiently large receiver array, the source strength q_{TEA} – describing the power being emitted by a source at a location **r** – can be estimated:

$$q_{TEA}(\boldsymbol{r},t) = \frac{4\pi}{N}\sum_{i=1}^{N}|\boldsymbol{r}_i-\boldsymbol{r}|p\left(\boldsymbol{r}_i, t-\frac{|\boldsymbol{r}_i-\boldsymbol{r}|}{c}\right) \quad (1)$$

where $p(\mathbf{r_i},t)$ is the pressure measured by the i^{th} array element (located at location r_i), N is the total number of array elements and c is the speed of sound in the medium ($c \approx 1500$m/s). The multiplication by $4\pi|\boldsymbol{r}_i-\boldsymbol{r}|$ accounts for the spherical spreading of the signal.

2) Robust Capon Beamforming (RCB)

The Robust Capon Beamformer, as detailed by Coviello et al in 2015 [9], builds on the conventional Capon beamformer. The Capon beamformer uses the same delay and sum algorithm used in TEA-PAM, but rather than weighting the contribution of each channel equally, RCB-PAM calculates a distinct weight for each channel to minimise variance, i.e., the energy of the delayed-and-summed signal. This is done by minimizing the coherence of signals across the array's channels, which can be expressed using the mean covariance matrix, R_s:

$$R_s = \frac{1}{K}\sum_t p(r_i,t)p(r_i,t)^T \quad (2)$$

Here, the superscript T is the transpose operation and the variable K represents the number of data in the time axis.

The weight applied to all channels can be written as a vector of the same length as the number of channels, called the weight vector. In Capon's beamformer, the sum of the weight vector is equal to unity. Hence, the coherent signal emitted from a point of interest will have a unity gain and thus will not be suppressed. This implies that the beamformer will not distort the amplitude of the signal coming from the point of interest. However, in practice, the signal emitted from the point will not be perfectly coherent. This is a result of many factors, including array imperfections, aberration, and slight misalignment of the investigated pixel with the true location of the source. These practical issues result in the suppression of the source's signal, reducing the signal-to-noise ratio of the beamformed image.

Thus, modifications were often introduced to Capon's beamformer to mitigate its low signal-to-noise ratio. RCB-PAM was one of the approaches developed to increase the robustness of the Capon beamformer [25]. In contrast to the original Capon beamformer, where there is no numerical limit on the weight vector, so no limit to the extent of suppression of signals, the RCB applies a constraint to this suppression, preserving imperfect signals from real sensors. Where the original Capon beamformer utilizes the weight vector, RCB introduces a steering vector a, having a unity mean, i.e. $\bar{a} = 1$. Unlike the weight vector, variations of numerical values of the elements of the steering vector are bounded by a variability parameter s. The limit on the variation of the steering vector 'tunes down' the suppression effect of the beamformer, preventing the suppression of imperfect signals. This improves the signal-to-noise ratio while maintaining superior resolution to that of TEA-PAM. The steering vector a for a given image pixel p can be found by solving the following constrained optimization problem:

$$\min(a^T R_s^{-1} a) \quad s.t. |a-\bar{a}|^2 \leq \epsilon \quad (3)$$

The solution to this problem is $a = \bar{a} - R_s^{-1}\bar{a}$. This requires the inverse of the covariance matrix, which can be calculated by using eigenvalue decomposition ($R_s = UV\,U^T$, where the decomposed matrix U and V contain the left and right singular vectors, respectively). The solution can then be reduced to the following:

$$\hat{a} = \bar{a} - U(I+\lambda V)^{-1}U^T\bar{a} \quad (4)$$

Here, I is the identity matrix and λ is the Lagrange multiplier of the constraint, which can be found with a few iterations of Newton's method.

Finally, the calculated steering vector is then scaled to produce $\hat{a}_0 = \frac{\hat{a}N}{||\hat{a}||}$. This ensures unambiguity in the source energy estimation. The source strength, q_{RCB}, can be estimated in a similar manner to that of TEA-PAM, but with the steering vector incorporated:

$$q_{RCB}(\boldsymbol{r},t) = \frac{4\pi}{N}\sum_{i=1}^{N}|\boldsymbol{r}_i-\boldsymbol{r}|\hat{a}_{0,i}(\boldsymbol{r})p\left(\boldsymbol{r}_i, t-\frac{|\boldsymbol{r}_i-\boldsymbol{r}|}{c}\right) \quad (5)$$

3) Axial Temporal Position (ATP)

Our ATP-PAM algorithm exploits the short duration of therapeutic wavelets, which are used in RaSP sequences and other therapeutic sequences. With a short wavelet, the time window where reradiated signals from each location would be captured by a sensor can be estimated, allowing for a pulse-

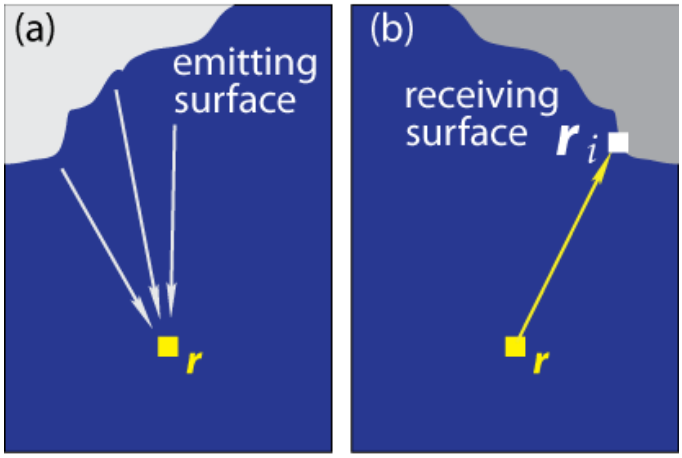

Fig. 1. **Time of flight information used in the axial temporal position algorithm.** This time is the summation of the (a) time that the primary sonication pulse travels from the emitter to the location of interest (position r) and (b) the time that the radiated acoustic emission from the location of interest travels to the receiving surface (r_i)

echo-like imaging modality to be used. This contrasts with other described passive algorithms, which use signals captured during the whole sonication duration. The time taken for signals to travel from locations where stimulated acoustic sources are present is captured by a sensor. The time of flight is the summation of the time it takes for the pulse to travel from the emitter to a target position **r** (T_{f1}; Figure 1a), and that for the reradiated pressure to travel from the position **r** to the array element located at position $\mathbf{r}_i$ (T_{f2}; Figure 1b), i.e. $T_f = T_{f1} + T_{f2}$. The first travel time is dictated by the transducer and its geometry, which can be simulated or measured using a hydrophone. The second travel time can be calculated as the distance from **r** to $\mathbf{r}_i$ divided by the speed of sound of the material. Furthermore, we assume that the bubbles will emit sound for a duration, T_{signal}, which will be approximately equal to the duration of the pulse (i.e., the pulse length).

The source strength q_{ATP} at a location **r** can be estimated from the pressure measurements, p(t), for a particular time window.

$$q_{ATP}(\boldsymbol{r},t) = \frac{4\pi}{N}\sum_{i=1}^{N}|\boldsymbol{r}_i-\boldsymbol{r}|p\left(\boldsymbol{r}_i, t-\frac{|\boldsymbol{r}_i-\boldsymbol{r}|}{c}\right) \quad (6)$$

when $T_f \le t-\frac{|\boldsymbol{r}_i-\boldsymbol{r}|}{c} \le T_f + T_{signal}$, otherwise $q_{ATP}(\boldsymbol{r},t) = 0$

4) Source Strength and Energy Maps

The source strength q(**r**,t) is a time-domain measurement at a specific point, **r**, and is fundamental to all passive acoustic mapping algorithms. This signal may be processed and analysed in either the time or frequency domains to determine the type, magnitude, and duration of cavitation produced at a particular point. Several methods of signal processing could be applied to the source strength signal, and include the extraction of sub-harmonic, harmonic, and ultra-harmonic signals or broadband noise.

A useful method is to generate an image of the source strength's energy:

$$E(\boldsymbol{r}) = \int \frac{q^2(\boldsymbol{r},t)}{4\pi\rho_0 c}dt \quad (7)$$

where ρ_0 is the nominal density of the medium.

Depending on the sensor arrangement, this can create a 2-dimensional or a 3-dimensional acoustic energy map. Note that due to the eigenvalue decomposition of the covariance matrix in the RCB-PAM case [30], [31], the energy for the RCB-PAM case, equivalent to the former, can also be written in a simplified manner:

$$E_{RCB}(\boldsymbol{r}) = \frac{|\boldsymbol{r}_i-\boldsymbol{r}|^2}{4\pi\alpha^2\rho_0 c}\cdot\frac{\Delta t}{\hat{a}_0^T(\boldsymbol{r})UV(\lambda^{-2}I+2\lambda^{-1}V+V^2)^{-1}U^T\hat{a}_0(\boldsymbol{r})} \quad (8)$$

where Δt is the sampling period.

5) Assumptions

For a focused transducer, the time it takes for the pulse to travel from the emitter to the point of interest, T_{f1}, is not easily calculated. In our implementation, we simplified this calculation by assuming that the emitted wavelet travelled as a plane wave within the therapeutic ultrasound beam. This was reasonable given the F-number of our transducer (0.67). With this assumption, T_{f1} only changed along the axial direction. When comparing our approximated T_{f1} to the true T_{f1} values captured using a needle hydrophone, the error was less than 0.3mm. Thus, for our transducer's geometry, and center frequency, our assumption produced low errors. However, a plane-wave assumption may not hold for all transducer arrangements, geometries, and center frequencies.

B. Simulations

Simulations were used to develop the ATP-PAM algorithm and test its performance with different acoustic sources and pulse lengths.

1) Simulation setup

The 2D simulations were performed in Matlab using the k-wave toolbox [52]. Acoustic sources were simulated as either emitting sources or as points that scattered an emitted acoustic wavelet. For both simulations, we modelled a linear imaging array that was placed at the top of the simulation grid. For the point scatterer simulation, a single-element therapeutic transducer was axially aligned to the linear array. The simulation grid was 800 by 800 with a grid-element spacing of 0.1 mm. The medium parameters were set to c_0 = 1,500 m/s (speed of sound), ρ_0 = 1,000 kg/m^3 (medium density), α_0 = 0.75 dB MHz^{-1}cm^{-1} (alpha absorption coefficient) and y = 1.5 (alpha power) [53]. The sampling frequency was set to 100 MHz and the number of simulation time points was set to 8,000, which corresponded to a total simulation time of 80 μs.

A 128-element linear receiver array was defined along a straight line, 2.5 mm from the top of the grid and centered laterally. Each sensor element had two non-sensor grid elements between them, resulting in a 0.3-mm distance between the midpoint of each sensor element. The single-element spherical-segment therapeutic transducer (focal depth: 60.5 mm, diameter: 90 mm) was modelled as an array of acoustic sources and positioned to focus a beam 30 mm away from the linear array. The top of the curved source was positioned 2.5 mm from the top of the grid and centered laterally. The transducer radius was 30 mm with a focus position 30 mm from the linear array and centered laterally. This provided a focal point at (x, z) = (0 mm, 30 mm), where x corresponded to the lateral distance from the central

axis of the linear array and z corresponded to the axial distance from the array.

Acoustic sources were modelled as point scatterers by defining points on the grid with a high acoustic impedance (ρ_m = 10,000 kg/m^3, c_m = 2000 m/s). This caused the emitted wavelets to scatter, with some of the energy returning back to the sensor array. Four point scatterers were placed as a grid at (x, z) = (-1.0 mm, 29 mm), (1.0 mm, 29 mm), (-1.0 mm, 31 mm), (1.0 mm, 31 mm). Point scatterers were exposed to 1-, 2-, and 5-cycles wavelets with a center frequency of 1 MHz.

Sources that emitted sound were placed at 100 randomly generated points within a rectangular grid (axial range: 10 mm to 70 mm, lateral range: -19.2 mm to 19.2 mm). In this setup the randomly positioned acoustic sources each emitted a wavelet at the same time. The linear array was used to passively acquire the emissions generated by the acoustic sources. The acoustic source simulations only used 1-cycle wavelets.

The acoustic sources and the focused transducer emitted a pre-defined waveform that was comparable to the acoustic emissions from microbubbles undergoing cavitation. Microbubbles have a characteristic frequency spectrum with peaks at frequencies corresponding to the harmonics of the base transducer frequency [54]. To mirror this, emission signals were designed by summing sine waves at the 3rd, 4th, 5th, 6th, and 7th harmonics of the 1 MHz transducer and limiting the signals to a duration of 1, 2, or 5 cycles of the base 1-MHz frequency.

2) Beam formation

Acoustic maps were generated using the ATP-PAM, RCB-PAM and TEA-PAM algorithms. The value of 0.01 was used for the tunable value, ϵ. The value was found by iterations and resulted in minimal signal in regions where the sources or reflectors were not present. The ATP-PAM algorithm was modified according to how the microbubbles were modelled. In the case of point scatterers the emission had to travel from the transducer to the point and back to the array, whereas an emission from the emitting sources only had to travel from the source to the array. This was accounted for in the ATP-PAM algorithm by multiplying the projected axial distance by two for a given time point in the source simulations. Acoustic maps were assessed across the 3 algorithms for the ability to revolve individual bubbles (point scatterers and emitters) and for the suppression of tail artefacts.

C. In vitro experiments

The aim of the in vitro experiment was to compare how well the PAM algorithms – TEA, RCB, and ATP – could resolve two, closely-placed objects. Acoustic wavelets were applied to two thin tubes containing microbubbles. Using wavelets of different pulse lengths, we ran the three algorithms to generate maps of the microbubble activity and evaluated how well each algorithm could resolve them.

1) Ultrasound transducers

An L7-4 linear array (number of elements: 128 elements, aperture size: 38.1 mm, element spacing: 0.298 mm) was placed through a rectangular cut-out of a single-element, focused ultrasound transducer (center frequency: 1 MHz, focal depth: 60.5 mm, active diameter: 90 mm, central rectangular opening: 30 mm x 70 mm; model number H-198, Sonic Concepts, Bothell, WA, USA). The transducer's beam had a FWHM axial length of 20 mm, a FWHM lateral width of 2 mm, and a FWHM elevational width of 1 mm. The focused transducer was driven by a function generator (33500B, Keysight, Santa Rosa, CA) through a power amplifier (2100L, Electronics and Innovation, Rochester, NY) and matching network. The linear array was connected to an ultrasound imaging engine (Vantage, Verasonics, Kirkland, USA). Both the function generator and imaging engine were controlled by a PC. A trigger signal was used to synchronize the linear array recordings and the emissions from the focused transducer. The linear array and focused transducer were mounted on a PC-controlled 3D positioning system and held in a water tank of degassed and deionized water. An acoustic absorber was placed at the bottom of the tank to limit acoustic reflections.

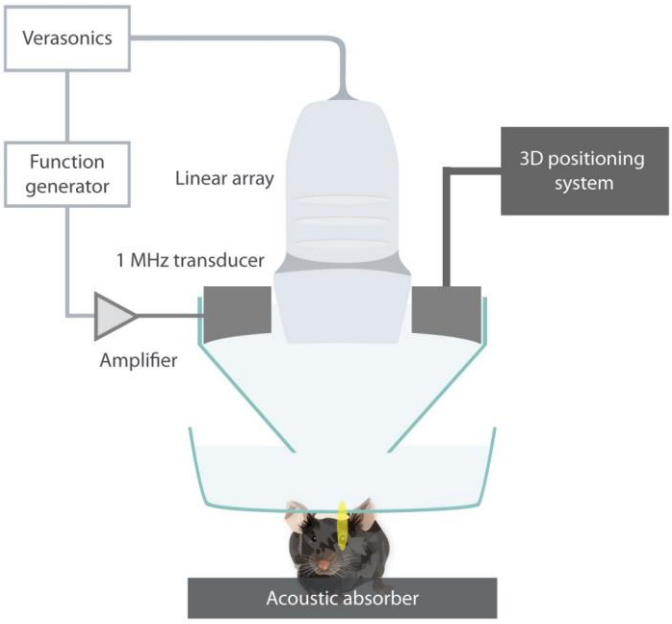

Fig. 2. **In vivo experimental setup.** The mouse brain was exposed to 1-MHz ultrasound emitted in a rapid short-pulse (RaSP) sequence. Pulses were emitted onto the left hippocampus through the intact scalp and skull. An L7-4 linear array coaxially aligned with the therapeutic transducer was used to capture the acoustic emissions generated by the microbubbles. The transducers were moved using a 3D positioning system to target the left hippocampus. The RaSP ultrasound sequence was produced by the function generators, passed through an amplifier and emitted via the transducer. Both emission and acquisition pathways were triggered using a Verasonics system.

2) Experimental setup

The resolution of the PAM algorithms was evaluated using two thin tubes (inner diameter: 0.28 mm; outer diameter: 0.61 mm) suspended in water. The tubes were held parallel to the array's surface, at approximately the focal distance of the focused transducer, and with a 2.5 mm separation distance between the center of each tube. The tubes were immobilized by threading them through holes of two custom 3D printed blocks. A raster scan using the focused transducer in pulse-echo

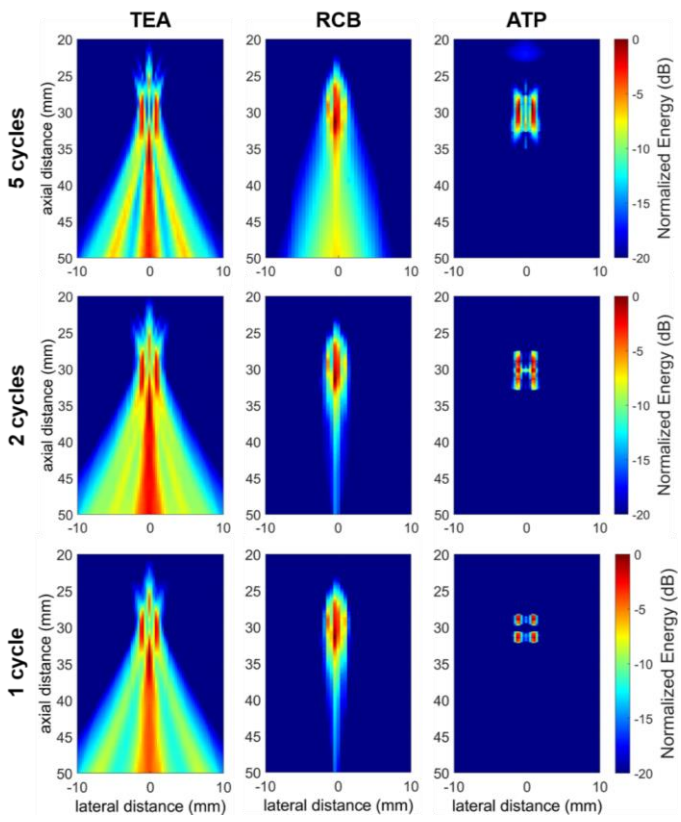

Fig. 3. **Simulated passive acoustic energy maps of four scattering points exposed to 5-, 2- and 1-cycle wavelets.** Four scattering points were defined in k-wave's Matlab toolbox and were exposed to a focused ultrasound beam with its focus in the center between the four reflective points. This was repeated for 5, 2 and 1 pressure cycles with a 1 MHz driving frequency. The sensor data was recorded by a 128-element linear array spanning across the axial distance. This was repeated for each number of cycles and the sensor data was reconstructed independently using (left) time exposure acoustics (TEA), (middle) robust Capon beamformer (RCB) and (right) axial temporal position passive acoustic mapping (ATP-PAM) algorithms.

mode was performed to confirm that the focal point of the transducer's beam was between the two tubes. SonoVue® microbubbles (Bracco, Milan, Italy) were infused into two thin tubes. Using the linear array, a B-mode image was used as a reference image for future analysis.

3) Protocol

The focused transducer emitted an acoustic wavelet with a 1 MHz center frequency and had an approximate pulse length of 1 µs at 1 cycle, 2 µs at 2 cycles, and 5 µs at 5 cycles. Two wavelets were emitted with a 500 ms pulse interval and comprised a single burst. For each pulse length, 125 bursts were emitted with a burst repetition frequency (BRF) of 0.5 Hz and a peak-rarefactional pressure of 0.6 MPa. SonoVue® (Bracco, Milan, Italy) microbubbles were diluted in a ratio of 1:100 (mean diameter: 2.5 µm [55]). The solution was flowed through the two tubes using a dual syringe pump at a flow rate of 5µL/s. The tubes with water only acted as a control and were used to ensure that acoustic emissions mapped by the algorithms were not due to the reflection from the tube alone.

4) Image processing and analysis

Due to the low concentration of microbubbles used, the energy of acoustic emissions generated by the microbubbles varied depending on whether bubbles were present in each tube. We selected acoustic emissions data that had an approximately equal energy generated from both tubes. This data was then used to reconstruct acoustic maps using the ATP, RCB, and TEA-PAM algorithms. These maps were then overlaid with lines to represent the tube walls, the position of which was extracted from the original B-mode images, to evaluate whether the acoustic activity was located within the tubes.

D. In vivo experiments

The purpose of the in vivo experiments was to evaluate whether acoustic emissions in the mouse brain could be localized within the skull cavity using the ATP-PAM algorithm.

1) Animals

Five female C57bl/6 wild type mice (age: 8-12 weeks, mass: 18.9 +/- 0.7 g; Envigo, Huntingdon, UK) were anaesthetized with 1.5% vaporized isoflurane (Zoetis UK Limited, London, UK) mixed with oxygen (0.8 L/min) using a vaporizer (Harvard Apparatus, Cambridge, UK). All protocols were approved by our local institutional animal facility committee and the UK Home Office regulatory establishments (PPL: 70/8585).

2) Model drug and microbubbles

SonoVue® (Bracco, Milan, Italy) microbubbles were injected into the tail vein (5 µl/g) 10 s after ultrasound emission was started. The microbubbles were activated according to the manufacturer's instructions to maintain their stability and were used within 6 hours of activation. Lysine-fixable 3-kDa dextran (concentration: 30 µg/g of body mass; Life Technologies, Paisley, UK) with a fluorescent tag (Texas Red®) was diluted in 100 µl phosphate buffered saline (PBS) and intravenously injected 30 seconds after the start of sonication.

3) Ultrasound transducers

The same ultrasound transducers and driving circuits used in the in vitro experiments were used for the in vivo experiments (Fig. 2).

4) Sonication protocol

Following the removal of fur from the mouse's head, each mouse was weighed and immobilized in a stereotaxic frame (World Precision Instruments, Hertfordshire, UK). A bath with a paraffin membrane bottom was filled with degassed water and placed on the mouse head while the two surfaces were coupled with an ultrasound gel. Once the cone of the ultrasound system was lowered into the water, the focal point of the transducer was positioned 3 mm beneath the skull using the transducer in pulse-echo mode to locate the skull (Fig. 2).

Using a previously described method [48], the left hippocampus was targeted while the right hippocampus was used as a control. Ten seconds after starting the ultrasound sonication, microbubbles were administered into the tail vein using a 30G catheter over a duration of half a minute. Mice were sonicated using a RaSP sequence. A wavelet (peak-negative

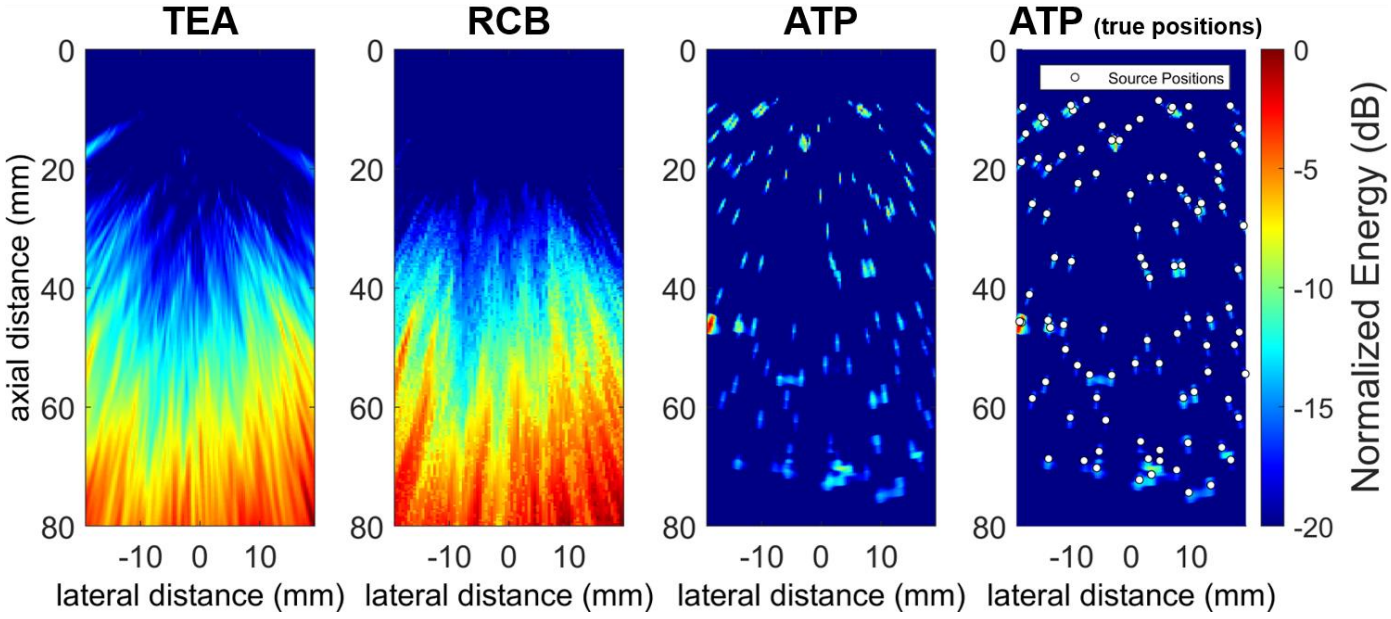

Fig. 4. **Simulated passive acoustic energy maps of 100 randomly positioned ultrasound sources with three different algorithms.** Time exposure acoustics (TEA), robust Capon beamformer (RCB) and axial temporal position (ATP) passive acoustic mapping reconstructions of simulated sensor data collected from 100 randomly positioned ultrasound sources in a rectangular grid in MATLAB toolbox K-wave. The ultrasound sources emitted a 1-cycle pressure wave with a 1-MHz center frequency and the data was recorded by a 128-element linear array extending across the lateral distance. True source positions can be viewed overlaid on the ATP reconstruction (right).

pressure: 535 kPa, center frequency: 1 MHz, pulse length: 1 cycle) was emitted in a rapid burst (pulse repetition frequency (PRF): 1.25 kHz, burst length (BL): 10 ms) that was repeated at a slow rate (burst repetition frequency (BRF): 0.5 Hz, number of bursts: 126). The peak-negative pressure reported here takes into account an 11% attenuation through the mouse skull [48]. These parameters were chosen based on the simulation and in vitro results, which showed the best resolution for ATP-PAM was with a 1-cycle wavelet. Parameters such as PRF, BL and BRF were chosen based on results obtained from previous in vivo work [48].

5) Histology and microscopy

After sonication, the mice were transcardially perfused with 20 mL PBS and 20 mL 10% formalin (Sigma Aldrich, St Louis, MO). The brains were removed from the skull, placed in 15% sucrose for 6 h and 30% sucrose overnight, and embedded in an optimum cutting temperature compound (OCT; Agar Scientific, Stansted, UK). The brain was then sectioned into 30 µm-thick coronal slices. Fluorescence microscopy images were acquired (10x; Zeiss Axio Observer, Oberkochen, Germany). The Texas Red molecular probes were excited at 562/40 nm and emissions were filtered at 624/40 nm.

6) Image processing and analysis

Regions of interest were selected around the left (treated) and right (control) hippocampi using MATLAB R2018b (Mathworks, Natick, MA). The normalized optical density (NOD) was quantified as a measure of the increase in fluorescence in the treated region compared to the control region. Pixel intensities higher than twice the standard deviation of the control region were summed and the sum in the control region was subtracted from the sum in the treated region. If the NOD was at least 1 standard deviation above the mean of the control region then the dextran delivery was considered successful.

For each mouse, the area of microbubble activity was quantified from both the cumulative energy maps and the maps with the highest cavitation energy to compare the three algorithms. This area was calculated from the PAM maps by summing all pixels with values above 25% of the maximum across all cumulative maps. To compare the three algorithms, the receiver data with the highest cavitation energy for each mouse, corresponding to an individual ultrasound pulse, was chosen for reconstruction and the area was calculated by summing all pixels with values above 25% of the maximum for each of these maps.

III. RESULTS

A. Simulations

Simulations were used to develop the ATP algorithm, test its performance against existing PAM algorithms and evaluate the effect of pulse length on imaging resolution. It included four point scatterers placed near the focal point of a focused beam, and 100 randomly positioned acoustic sources.

For all pulse lengths tested (1, 2, and 5 cycles), TEA-PAM was able to resolve the point scatterers laterally, but not axially. TEA-PAM produced tail artefacts, which overestimated the acoustic energies in regions prior and after the true scattering points. The tail artefact extended from the points clustered at around 30 mm from the transducer to the end of the reconstructed field of view (60 mm). The tail artefact created energy peaks that may be incorrectly identified as acoustic sources, which appeared between the columns of scatters, both proximal and distal to the transducers. RCB-PAM was able to partially suppress the tail artefact, especially with 2 and 5 cycles where the energy from the reflective points were higher.

However, RCB-PAM was not able to resolve the four scattering points laterally or axially. Also, RCB-PAM generated false acoustic sources, which distorted the overall map, hiding the location of the true sources.

With a 1-cycle pulse, ATP-PAM was able to resolve all four reflective points, which implies a horizontal and axial resolution limit better than 2 mm. At 2 and 5 cycles, ATP-PAM was unable to resolve the reflective points axially but was able to resolve the points horizontally. At 1, 2, and 5 cycles ATP-PAM had no tail artefact and no false scattering points (Fig. 3).

Both TEA-PAM and RCB-PAM were unable to resolve the acoustic sources, because of the overwhelming accumulation of tail artefacts throughout the image (Fig. 4). ATP-PAM was able to suppress the tail artefacts and resolve many of the 100 sources. Approximately uniform energy values for every source were also observed, indicating that the beamformer minimally distorted the sources' energy. The lateral resolution of the image degraded with distance from the imaging array, which is expected of delay-and-sum beamformer. The axial resolution was unaffected by the sources' axial positions.

B. In vitro experiments

The in vitro experimental work evaluated the feasibility of the ATP-PAM algorithm and qualitatively compared the ATP-PAM algorithm to existing PAM algorithms. Two thin tubes, whose centers were separated by 2.5 mm, were perfused with microbubbles and sonicated by focused ultrasound pulses of 1, 2, or 5 cycles. Acoustic emissions generated by the microbubbles were then captured with a linear array.

The axial resolution of ATP-PAM images was dependent on the pulse length. ATP-PAM was able to resolve the two tubes with pulse lengths of 1 and 2 cycles, but not 5 cycles (Fig. 5). In contrast, both TEA-PAM and RCB-PAM could not resolve the two tubes in any of the pulse lengths tested. Tail artefacts were eliminated with ATP-PAM for all pulse lengths tested, but remained present with TEA-PAM and RCB-PAM.

C. In vivo experiments

A single-cycle pulse in a RaSP sequence was able to deliver a model drug across the BBB. An increase in fluorescence above the autofluorescence intensity was significant in the targeted, left hippocampus (Fig. 6). On the contralateral brain hemisphere, where no ultrasound was applied, no significant increase in fluorescence was detected. ATP-PAM revealed cavitation activity within the brain tissue and no cavitation activity was detected outside the ultrasound beam. The position of cavitation activity on the ATP-PAM images matched the location of drug delivery in all five mice. However, there were regions where the drug was delivered, but where only a low level of cavitation activity was detected. The following areas of cavitation activity for the five mice were calculated from the cumulative ATP-PAM maps: 4.3 ± 4.6 mm^2. In contrast, TEA-PAM and RCB-PAM produced energy values of acoustic emissions outside the mouse brain and ultrasound beam where cavitation activity was unlikely to be generated (Fig. 7). The areas of activity calculated from RCB-PAM (9.44 ± 5.49 mm^2) and TEA-PAM (72.84 ± 50.33 mm^2) maps of single pulses were found to be significantly higher than those of ATP-PAM (1.23 ± 0.21 mm^2; $P < 0.01$). The area of the brain overlapping with the ultrasound beam is approximately 7.8 mm^2, which shows that the area of activity calculated from the ATP-PAM maps was within this range, while with TEA and RCB-PAM it was not.

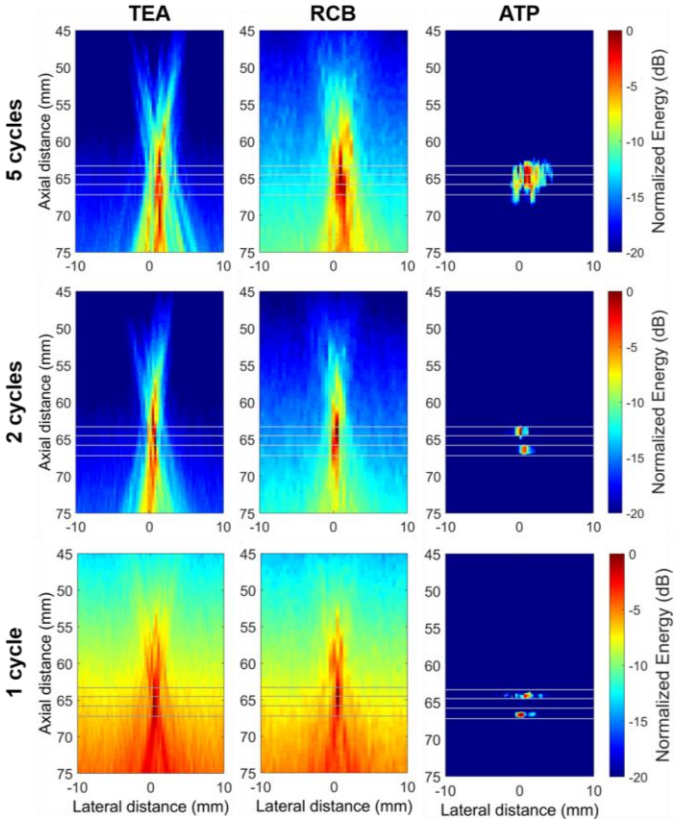

Fig. 5. In vitro passive acoustic energy maps of microbubbles within two thin tubes exposed to 5-, 2- and 1-cycle wavelets. Microbubbles were injected through two thin silicone tubes (0.28 mm internal diameter and 0.61 mm external diameter) at approximately 2.5 mm axial separation and sonicated by 1-MHz center frequency pressure cycles with a beam focus at the axial midpoint of the two thin tubes. The resulting cavitation emissions were captured by a 128-element L7-4 linear array, which was embedded in the center of the ultrasound transducer. Axial distances refer to the distance from the linear array. The captured sensor data for 5, 2 and 1 pressure cycles was reconstructed independently using time exposure acoustics (TEA), robust Capon beamformer (RCB) and axial temporal position (ATP) passive acoustic mapping algorithms. The four horizontal lines show where the two thin tubes are located based on the B-mode image and have been overlaid with the TEA, RCB, and ATP reconstructions for 5, 2 and 1 pressure cycles.

IV. Discussion

We have demonstrated that therapeutic acoustic wavelets and the ATP algorithm can resolve distinct acoustic sources, extract the source strength values and eliminate tail artefacts observed in other PAM algorithms. The axial resolution of ATP-PAM depends on the pulse length of the therapeutic wavelet, which degrades with increasing pulse lengths. This implies that ATP-PAM is suitable for therapeutic wavelets or other short-pulse waveforms (e.g., histotripsy). TEA-PAM and RCB-PAM can be used for very long therapeutic pulses including continuous wave sonication, because they are not dependent on time-of-flight estimations. However, new therapeutic sequences are

being developed that use short pulse lengths, such as a RaSP sequence study that used 5 cycles [40], [44], [45], [48]. In the present study, we have demonstrated a therapeutic response – brain drug delivery – using a single-cycle acoustic wavelet. Thus, there is considerable scope now, and in the future, as new sequences are developed, to use therapeutic wavelets for imaging. In our simulations, ATP-PAM showed an improved axial resolution for both 1- and 2-cycle pulses, with the added benefit of tail artefact suppression for all pulse lengths tested (Fig. 3-4). The simulated reconstruction in figure 3 showed that with a single-cycle wavelet, ATP-PAM could resolve each point individually within the cluster, whereas TEA and RCB could not. The simulation results also showed that as expected, RCB-PAM suppressed some of the tail artefact present in TEA-PAM. However, ATP-PAM had no tail artefacts, because the spatial positions on the image were inherently linked with temporal positions in the data. Thus, any interference of reflections from point scatterers further down the image were not incorrectly added to the image. The cumulative effect of tail artefacts can be observed in the 100 random acoustic source simulation (Fig. 4), where due to the large number of sources, both TEA and RCB experienced an accumulation of tail artefacts making it difficult to locate any sources, biasing the energy prediction towards the bottom of the image. In contrast, ATP-PAM maintained source energy predictions that were unbiased with distance and correctly localized most of the 100 sources. These points are reinforced by the in vitro results in figure 5, which show that with ATP-PAM the two tubes at 2.5 mm distance from each other could be resolved at 1 and 2 cycles but could not at 5 cycles and with RCB and TEA-PAM. In future work, we intend to expand the simulation work to encompass 3D maps, moving sources and multiple emitters which are being used in human and primate BBB opening studies [56]–[58]. This will allow us to evaluate further the robustness of ATP-PAM in realistic scenarios.

In previous studies, the lowest pulse length shown to deliver drugs to the brain with a RaSP sequence was with 2.3 and 5 cycles [42], [48]. Here, for the first time, we have demonstrated drug delivery with the RaSP sequence using only a single-cycle pulse. Through the human skull, we would still expect to detect single cycles based on previous studies [59]. We also showed that ATP-PAM could be incorporated in the RaSP sequence and enabled not only the monitoring of acoustic activity, but also the ability to be resolve acoustic events both within the ultrasound beam and the mouse brain. The ATP cumulative maps showed microbubble activity in the region where the highest pressure within the focal beam was located. This also corresponded to regions where high drug delivery was detected. However, in some regions where our model drug was present, no acoustic activity was detectable and vice versa. A one-to-one correlation between the activity and drug delivery was therefore not observed. However, we did not expect that such a correlation would occur for several reasons. First, an ultrasound beam and poly-sized microbubbles are likely to produce a wide range of cavitation activity. Therefore, it is unlikely that every microbubble that radiates sound will also produce a drug delivery event. Second, once the drug is delivered across the blood vessels, it will diffuse to regions where there is no microbubble activity in the first place. The mass transport of drug following sonication cannot be accounted for by the acoustic data. Third, there is a thickness mismatch between our acoustic map and that of the fluorescent image. The elevational focus of our receiver is in the order of millimeters, whereas the brain slices we cut are 30 µm-thick. We found that many of these brain slices had a different drug delivery distribution. The ATP-PAM images reflect the acoustic energy from many of these slices stacked together, therefore a comparison between one sample slide and the overall acoustic map may not yield a perfect correlation. In the future, a comparison of a 3D drug delivery volume to a 3D ATP-PAM image would be more informative. Fourth, the acoustic data may come from non-

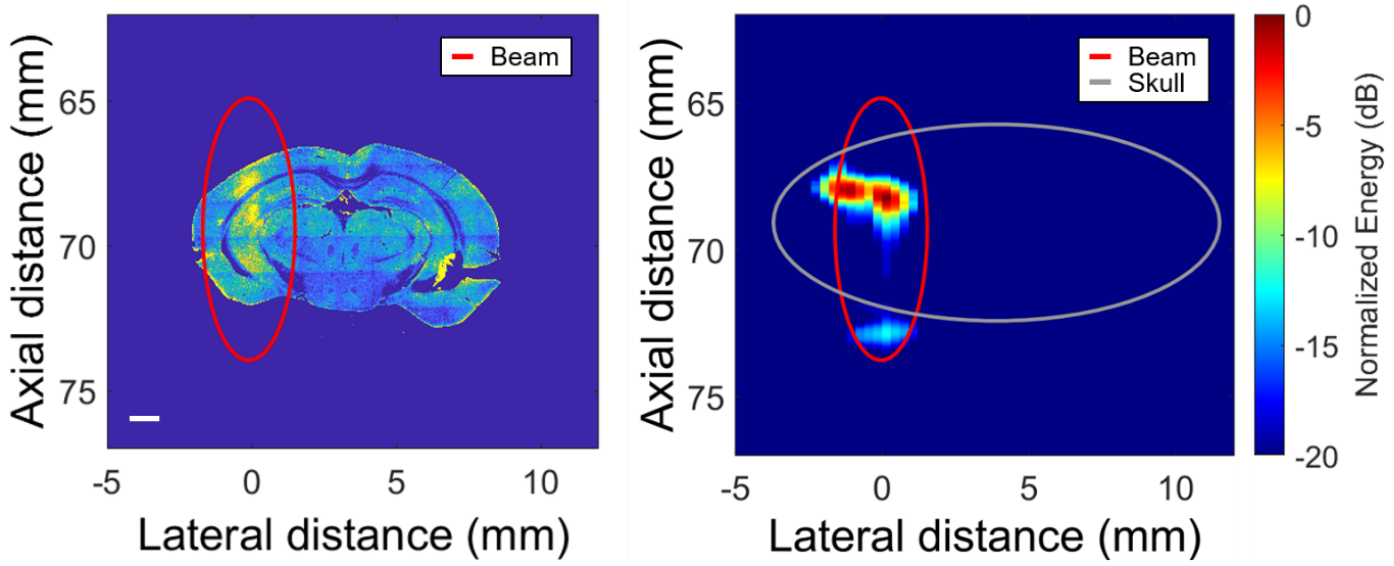

Fig. 6. **In vivo drug delivery and cumulative acoustic map of a mouse brain exposed to a 1-cycle rapid short-pulse (RaSP) sequence.** (Left) The fluorescence image shows a single slice where dextran is delivered to the left hippocampus of a mouse brain using a RaSP sequence (centre frequency = 1.25 MHz; peak negative pressure = 535 kPa; pulse length = 1 cycle; pulse repetition frequency = 1.25 kHz, burst repetition frequency = 0.5 Hz; ultrasound beam shown as a red ellipse). (Right) The cumulative acoustic map reconstructed using axial temporal position passive acoustic mapping (ATP-PAM) shows where microbubble activity was detected within the mouse skull (grey ellipse). The scale bar indicates 1 mm.

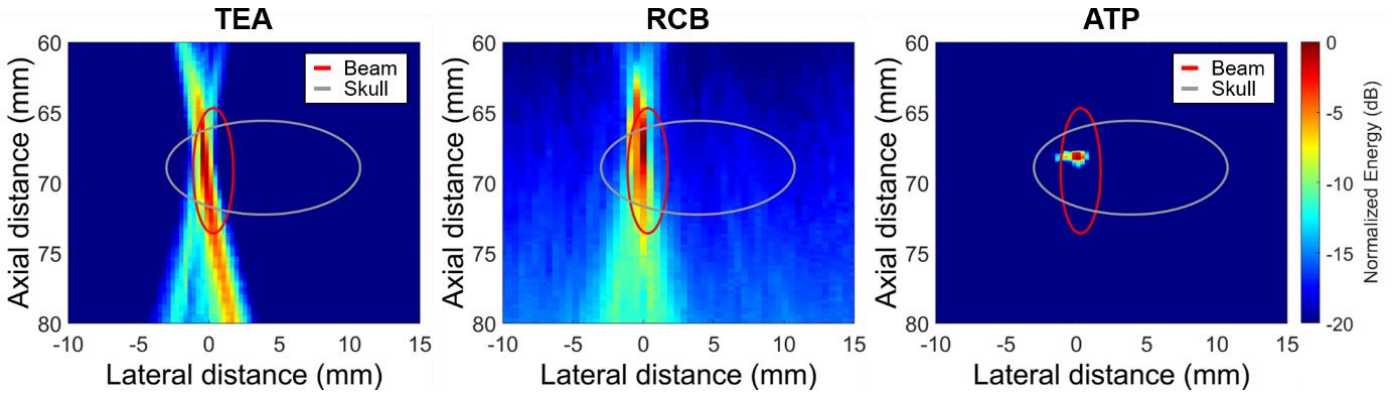

Fig. 7. **In vivo acoustic maps reconstructed comparing three different algorithms.** Time exposure acoustics (TEA), robust Capon beamformer (RCB) and axial temporal position (ATP) passive acoustic mapping reconstructions of a single pulse from in vivo data. (Left) TEA and (center) RCB maps show tail artefacts while (right) ATP-PAM shows no tail artefact and an improved axial resolution. The red ellipse represents the ultrasound beam while the grey ellipse delineates the mouse skull.

bubble sources, which have no associated therapeutic effect. For example, the activity observed at the very bottom of the focal region, outside of the brain ellipse (Fig. 6), is thought to be due to the nonlinear propagation, air in the gel beneath the mouse head, or the microbubble's acoustic emissions reflecting within the skull cavity. One of the advantages of ATP-PAM is that its axial resolution is dependent on the pulse length rather than the aperture. In TEA-PAM and RCB-PAM, the axial resolution can be improved by increasing the effective aperture size (.e., use a wider linear array or move the linear array closer to the acoustic sources). However, there are practical limits to the width of the aperture and how close the linear array can be placed to the region of interest. ATP is primarily dependent on the pulse length of the acoustic wavelet and is thus effective both close and further away from the region of interest.

The areas of microbubble activity calculated from ATP-PAM maps were found to be within the expected area sonicated within the brain, while the areas from RCB and TEA-PAM maps significantly overestimated the region of drug delivery.

The ATP algorithm is computationally efficient when compared to the other PAM algorithms. When calculating the source strength of a pixel, the ATP algorithm is only applied to the short, relevant time window of the channel data. In contrast, TEA-PAM is applied to the entire channel data. RCB-PAM is more computationally intensive than both TEA-PAM and ATP-PAM, because it requires matrix inversions, which can cause computational times to grow exponentially with the number of array elements. Thus, TEA-PAM has already been implemented in real-time algorithms [27], [60], [61].

A potential limitation of the ATP algorithm is the limited information on spectral components of the signal. With long pulse sonications, spectral components, e.g. subharmonic signals, can be distinguished with good resolution. Filters can be applied to the signal prior or after beamforming to produce maps of energy in different spectral components. However, with the short pulse used with ATP, these features may not be easily distinguishable. There is therefore a trade-off between the image resolution and the ability to precisely identify different spectral components.

In the future, we aim to optimize the RaSP sequence and microbubbles to improve the drug delivery distribution and correlate acoustic activity to drug delivery. We will also optimize the pulse length for both improved drug delivery and imaging axial resolution. We also plan to incorporate the ATP-PAM algorithm to provide real-time control of trans-BBB delivery procedures.

One limitation of ATP-PAM is that it requires the knowledge of the location of the transducer relative to the region of interest, making ATP more difficult to implement than TEA or RCB. However, this time of flight from the transducer to pixel of interest can be measured experimentally with a hydrophone or predicted with computer simulations. We implemented a simple approach without exacerbating localization errors by assuming that ultrasound propagated as a plane wave in the focal volume. Furthermore ATP-PAM cannot be used for longer pulses, which may be required for several therapeutic applications, such as thermal ablation, hyperthermia, or sonothrombolysis. Moreover, ATP-PAM assumes that the duration whereby microbubbles generate acoustic emissions is equal in length to the sonication pulse length, but this may not always be the case. For example, there could be rebound signals, which would be incorrectly placed in distal pixels [62].

V. CONCLUSION

When using therapeutic wavelets (short-duration, low-pressure pulses), time-of-flight can be used to localize the strength and energy of acoustic sources. Our ATP-PAM algorithm extracts the source strength, improves the axial resolution of imaging, and eliminates tail artefacts present in RCB-PAM and TEA-PAM algorithms. ATP-PAM works best with short pulse lengths and degrades as the pulse length increases, eventually converging to the original TEA-PAM algorithm. Thus, ATP-PAM is only useful and relevant for therapeutic sequences that use short wavelets. We have also demonstrated that a single-cycle wavelet used in a RaSP sequence can deliver drugs across the BBB in mice; and that ATP-PAM can localize cavitation activity within the mouse brain. In conclusion, ATP-PAM can improve the accuracy and precision of monitoring therapeutic ultrasound procedures by

providing real-time, small-resolution, and tail-artefact-absent imaging.

ACKNOWLEDGMENTS

This work was supported by Alzheimer's Research UK (ARUK-IRG2017A-7). S.V.M. and M.J.C. were supported by the Engineering and Physical Sciences Research Council (EP/L015226/1; EP/L016737/1) and K.S. was supported by the Royal Thai Government Scholarship. This study used equipment from the Facility for Imaging by Light Microscopy (FILM) at Imperial College London, supported by funding from the Wellcome Trust (grant 104931/Z/14/Z). We would like to thank Javier Cudeiro Blanco for all his help with the simulations; Antonios N. Pouliopoulos for his kind explanations; Ahmed El Ghamrawy and Gerard Mir Hernandez for their help. We thank Dr Claire Higgins for the use of her cryostat and everyone in the NSB laboratory.

REFERENCES

[1] J. J. Choi, M. Pernot, S. A. Small, and E. E. Konofagou, "Noninvasive, transcranial and localized opening of the blood-brain barrier using focused ultrasound in mice," *Ultrasound Med. Biol.*, vol. 33, no. 1, pp. 95–104, 2007, doi: 10.1016/j.ultrasmedbio.2006.07.018.

[2] F. Stewart *et al.*, "A Prototype Therapeutic Capsule Endoscope for Ultrasound-Mediated Targeted Drug Delivery," *J. Med. Robot. Res.*, 2018, doi: 10.1142/s2424905x18400019.

[3] K. B. Bader, G. Bouchoux, and C. K. Holland, "Sonothrombolysis," *Advances in Experimental Medicine and Biology*. 2016, doi: 10.1007/978-3-319-22536-4_19.

[4] N. J. Abbott, A. A. K. Patabendige, D. E. M. Dolman, S. R. Yusof, and D. J. Begley, "Structure and function of the blood-brain barrier," *Neurobiology of Disease*. 2010, doi: 10.1016/j.nbd.2009.07.030.

[5] J. P. Patel and B. N. Frey, "Disruption in the blood-brain barrier: The missing link between brain and body inflammation in bipolar disorder?," *Neural Plasticity*. 2015, doi: 10.1155/2015/708306.

[6] W. M. Pardridge, "The blood-brain barrier: bottleneck in brain drug development.," *NeuroRx*, vol. 2, no. 1, pp. 3–14, 2005, doi: 10.1602/neurorx.2.1.3.

[7] W. M. Pardridge, "Blood-brain barrier drug targeting: the future of brain drug development.," *Molecular interventions*. 2003, doi: 10.1124/mi.3.2.90.

[8] S. Ohtsuki and T. Terasaki, "Contribution of carrier-mediated transport systems to the blood-brain barrier as a supporting and protecting interface for the brain; importance for CNS drug discovery and development," *Pharmaceutical Research*. 2007, doi: 10.1007/s11095-007-9374-5.

[9] W. M. Pardridge, "Biopharmaceutical drug targeting to the brain," *Journal of Drug Targeting*. 2010, doi: 10.3109/10611860903548354.

[10] W. M. Pardridge, "Re-engineering biopharmaceuticals for delivery to brain with molecular Trojan horses," *Bioconjugate Chemistry*. 2008, doi: 10.1021/bc800148t.

[11] K. Hynynen, N. McDannold, N. Vykhodtseva, and F. a Jolesz, "Noninvasive MR imaging-guided focal opening of the blood-brain barrier in rabbits.," *Radiology*, vol. 220, no. 3, pp. 640–646, 2001, doi: 10.1148/radiol.2202001804.

[12] B. Baseri, J. J. Choi, Y. S. Tung, and E. E. Konofagou, "Multi-modality safety assessment of blood-brain barrier opening using focused ultrasound and definity microbubbles: A short-term study," *Ultrasound Med. Biol.*, vol. 36, no. 9, pp. 1445–1459, 2010, doi: 10.1016/j.ultrasmedbio.2010.06.005.

[13] M. Kinoshita, N. McDannold, F. A. Jolesz, and K. Hynynen, "Noninvasive localized delivery of Herceptin to the mouse brain by MRI-guided focused ultrasound-induced blood-brain barrier disruption," *Proc. Natl. Acad. Sci.*, vol. 103, no. 31, pp. 11719–11723, 2006, doi: 10.1073/pnas.0604318103.

[14] J. Shin *et al.*, "Focused ultrasound–mediated noninvasive blood-brain barrier modulation: preclinical examination of efficacy and safety in various sonication parameters," *J. Neurosurg.*, vol. 44, no. 2, p. E15, 2018.

[15] J. R. Lindner, "Microbubbles in medical imaging: current applications and future directions.," *Nat. Rev. Drug Discov.*, vol. 3, no. 6, pp. 527–32, 2004, doi: 10.1038/nrd1417.

[16] N. Hosseinkhah and K. Hynynen, "A three-dimensional model of an ultrasound contrast agent gas bubble and its mechanical effects on microvessels," *Phys. Med. Biol.*, 2012, doi: 10.1088/0031-9155/57/3/785.

[17] R. E. Apfel, "Sonic effervescence: A tutorial on acoustic cavitation," *J. Acoust. Soc. Am.*, vol. 101, no. September 1996, p. 1227, 1997, doi: 10.1121/1.418130.

[18] T. G. Leighton, "The Acoustic Bubble," *J. Acoust. Soc. Am.*, vol. 96, p. 2616, 1994, doi: 10.1121/1.410082.

[19] J. Tu, T. J. Matula, A. A. Brayman, and L. A. Crum, "Inertial cavitation dose produced in ex vivo rabbit ear arteries with Optison® by 1-MHz pulsed ultrasound," *Ultrasound Med. Biol.*, 2006, doi: 10.1016/j.ultrasmedbio.2005.10.001.

[20] J. H. Hwang, J. Tu, A. A. Brayman, T. J. Matula, and L. A. Crum, "Correlation between inertial cavitation dose and endothelial cell damage in vivo," *Ultrasound Med. Biol.*, 2006, doi: 10.1016/j.ultrasmedbio.2006.07.016.

[21] J. Deng *et al.*, "The role of caveolin-1 in blood-brain barrier disruption induced by focused ultrasound combined with microbubbles," *J. Mol. Neurosci.*, 2012, doi: 10.1007/s12031-011-9629-9.

[22] N. McDannold, C. D. Arvanitis, N. Vykhodtseva, and M. S. Livingstone, "Temporary disruption of the blood-brain barrier by use of ultrasound and microbubbles: Safety and efficacy evaluation in rhesus macaques," *Cancer Res.*, 2012, doi: 10.1158/0008-5472.CAN-12-0128.

[23] T. Nhan, A. Burgess, E. E. Cho, B. Stefanovic, L. Lilge, and K. Hynynen, "Drug delivery to the brain by focused ultrasound induced blood-brain barrier disruption: Quantitative evaluation of enhanced permeability of cerebral vasculature using two-photon microscopy," *J. Control. Release*, 2013, doi: 10.1016/j.jconrel.2013.08.029.

[24] C. Coviello, J. Choi, J. Collin, R. Carlisle, M. Gyongy, and C. C. Coussios, "Passive acoustic mapping of stable and inertial cavitation during ultrasound therapy," *J. Acoust. Soc. Am.*, 2014, doi: 10.1121/1.4900321.

[25] C. Coviello *et al.*, "Passive acoustic mapping utilizing optimal beamforming in ultrasound therapy monitoring.," *J. Acoust. Soc. Am.*, vol. 137, no. 5, pp. 2573–85, 2015, doi: 10.1121/1.4916694.

[26] M. Gyöngy and C.-C. Coussios, "Passive cavitation mapping for localization and tracking of bubble dynamics," *J. Acoust. Soc. Am.*, vol. 128, no. 4, pp. EL175–EL180, 2010, doi: 10.1121/1.3467491.

[27] J. J. Choi, R. C. Carlisle, C. Coviello, L. Seymour, and C. C. Coussios, "Non-invasive and real-time passive acoustic mapping of ultrasound-mediated drug delivery," *Phys. Med. Biol.*, 2014, doi: 10.1088/0031-9155/59/17/4861.

[28] J. Li, P. Stoica, and Z. Wang, "On robust Capon beamforming and diagonal loading," *IEEE Trans. Signal Process.*, 2003, doi: 10.1109/TSP.2003.812831.

[29] S. Lu *et al.*, "Passive acoustic mapping of cavitation using eigenspace-based robust Capon beamformer in ultrasound therapy," *Ultrason. Sonochem.*, 2018, doi: 10.1016/j.ultsonch.2017.10.017.

[30] P. Stoica, Z. Wang, and J. Li, "Robust Capon beamforming," *IEEE Signal Process. Lett.*, 2003, doi: 10.1109/LSP.2003.811637.

[31] Z. Wang, J. Li, and R. Wu, "Time-delay- And time-reversal-based robust Capon beamformers for ultrasound imaging," *IEEE Trans. Med. Imaging*, 2005, doi: 10.1109/TMI.2005.857222.

[32] K. J. Haworth *et al.*, "Passive imaging with pulsed ultrasound insonations," *J. Acoust. Soc. Am.*, 2012, doi: 10.1121/1.4728230.

[33] V. A. Salgaonkar, S. Datta, C. K. Holland, and T. D. Mast, "Passive cavitation imaging with ultrasound arrays," *J. Acoust. Soc. Am.*, 2009, doi: 10.1121/1.3238260.

[34] E. Lyka, C. M. Coviello, C. Paverd, M. D. Gray, and C. C. Coussios, "Passive Acoustic Mapping Using Data-Adaptive Beamforming Based on Higher Order Statistics," *IEEE Trans. Med. Imaging*, 2018, doi: 10.1109/TMI.2018.2843291.

[35] S. D. Somasundaram, N. H. Parsons, P. Li, and R. C. De Lamare, "Reduced-dimension robust capon beamforming using Krylov-subspace techniques," *IEEE Trans. Aerosp. Electron. Syst.*, 2015,

doi: 10.1109/TAES.2014.130485.

[36] Z. Xi, X. F. Wu, S. Wu, Z. Tang, and S. Hu, "Low-complexity robust capon beamforming based on reduced-rank technique," *J. Electr. Comput. Eng.*, 2015, doi: 10.1155/2015/583075.

[37] M. T. Burgess, I. Apostolakis, and E. E. Konofagou, "Power cavitation-guided blood-brain barrier opening with focused ultrasound and microbubbles," *Phys. Med. Biol.*, vol. 63, no. 6, p. 065009, 2018.

[38] J. J. Choi, M. Pernot, T. R. Brown, S. A. Small, and E. E. Konofagou, "Spatio-temporal analysis of molecular delivery through the blood-brain barrier using focused ultrasound," *Phys. Med. Biol.*, 2007, doi: 10.1088/0031-9155/52/18/004.

[39] N. McDannold, N. Vykhodtseva, and K. Hynynen, "Blood-Brain Barrier Disruption Induced by Focused Ultrasound and Circulating Preformed Microbubbles Appears to Be Characterized by the Mechanical Index," *Ultrasound Med. Biol.*, 2008, doi: 10.1016/j.ultrasmedbio.2007.10.016.

[40] K. F. Bing, G. P. Howles, Y. Qi, M. L. Palmeri, and K. R. Nightingale, "Blood-Brain Barrier (BBB) Disruption Using a Diagnostic Ultrasound Scanner and Definity® in Mice," *Ultrasound Med. Biol.*, 2009, doi: 10.1016/j.ultrasmedbio.2009.03.012.

[41] J. J. Choi, K. Selert, Z. Gao, G. Samiotaki, B. Baseri, and E. E. Konofagou, "Noninvasive and localized blood-brain barrier disruption using focused ultrasound can be achieved at short pulse lengths and low pulse repetition frequencies," *J. Cereb. Blood Flow Metab.*, vol. 31, no. 2, pp. 725–737, 2011, doi: 10.1038/jcbfm.2010.155.

[42] J. J. Choi, K. Selert, F. Vlachos, A. Wong, and E. E. Konofagou, "Noninvasive and localized neuronal delivery using short ultrasonic pulses and microbubbles," *Proc. Natl. Acad. Sci. U. S. A.*, vol. 108, no. 40, pp. 16539–44, 2011, doi: 10.1073/pnas.1105116108.

[43] K. Hynynen, N. McDannold, H. Martin, F. A. Jolesz, and N. Vykhodtseva, "The threshold for brain damage in rabbits induced by bursts of ultrasound in the presence of an ultrasound contrast agent (Optison®)," *Ultrasound Med. Biol.*, 2003, doi: 10.1016/S0301-5629(02)00741-X.

[44] M. A. O'Reilly, A. C. Waspe, M. Ganguly, and K. Hynynen, "Focused-Ultrasound Disruption of the Blood-Brain Barrier Using Closely-Timed Short Pulses: Influence of Sonication Parameters and Injection Rate," *Ultrasound Med. Biol.*, vol. 37, no. 4, pp. 587–594, 2011, doi: 10.1016/j.ultrasmedbio.2011.01.008.

[45] B. Zhao *et al.*, "Blood-brain barrier disruption induced by diagnostic ultrasound combined with microbubbles in mice," *Oncotarget*, 2018, doi: 10.18632/oncotarget.23527.

[46] A. N. Pouliopoulos, C. Li, M. Tinguely, V. Garbin, M.-X. Tang, and J. J. Choi, "Rapid short-pulse sequences enhance the spatiotemporal uniformity of acoustically-driven microbubble activity during flow conditions," *J. Acoust. Soc. Am.*, vol. 140, no. 4, pp. 2469–2480, 2016.

[47] A. N. Pouliopoulos, S. Bonaccorsi, and J. J. Choi, "Exploiting flow to control the in vitro spatiotemporal distribution of microbubble-seeded acoustic cavitation activity in ultrasound therapy.," *Phys. Med. Biol.*, vol. 59, no. 22, pp. 6941–57, 2014, doi: 10.1088/0031-9155/59/22/6941.

[48] S. V. Morse *et al.*, "Rapid short-pulse ultrasound delivers drugs uniformly across the murine blood-brain barrier with negligible disruption," *Radiology*, 2019, doi: 10.1148/radiol.2019181625.

[49] O. Couture, M. Fink, and M. Tanter, "Ultrasound contrast plane wave imaging," *IEEE Trans. Ultrason. Ferroelectr. Freq. Control*, 2012, doi: 10.1109/TUFFC.2012.2508.

[50] M. Tanter and M. Fink, "Ultrafast imaging in biomedical ultrasound," *IEEE Trans. Ultrason. Ferroelectr. Freq. Control*, 2014, doi: 10.1109/tuffc.2014.6689779.

[51] M. Shen, Q. Zhang, D. Li, and J. Yang, "Beamspace sparse representation weighting beamforming for plane wave emission ultrasound instrument," in *Conference Record - IEEE Instrumentation and Measurement Technology Conference*, 2011, doi: 10.1109/IMTC.2011.5944109.

[52] B. E. Treeby and B. T. Cox, "k-Wave: MATLAB toolbox for the simulation and reconstruction of photoacoustic wave fields," *J. Biomed. Opt.*, 2010, doi: 10.1117/1.3360308.

[53] B. E. Treeby and B. T. Cox, "Modeling power law absorption and dispersion for acoustic propagation using the fractional Laplacian," *J. Acoust. Soc. Am.*, 2010, doi: 10.1121/1.3377056.

[54] S. K. Wu *et al.*, "Characterization of different microbubbles in assisting focused ultrasound-induced blood-brain barrier opening," *Sci. Rep.*, 2017, doi: 10.1038/srep46689.

[55] M. Schneider, "Characteristics of SonoVue™," *Echocardiography*, 1999, doi: 10.1111/j.1540-8175.1999.tb00144.x.

[56] T. Mainprize *et al.*, "Blood-Brain Barrier Opening in Primary Brain Tumors with Non-invasive MR-Guided Focused Ultrasound: A Clinical Safety and Feasibility Study," *Sci. Rep.*, 2019, doi: 10.1038/s41598-018-36340-0.

[57] D. McMahon, C. Poon, and K. Hynynen, "Increasing BBB Permeability via Focused Ultrasound: Current Methods in Preclinical Research," in *Neuromethods*, 2019.

[58] N. Lipsman *et al.*, "Initial experience of blood-brain barrier opening for chemotherapeutic drug delivery to brain tumours by MR-guided focused ultrasound," *Neuro. Oncol.*, vol. 19, no. 6, p. vi275, 2017.

[59] D. E. Soulioti, D. Espindola, P. A. Dayton, and G. F. Pinton, "Super-Resolution Imaging through the Human Skull," *IEEE Trans. Ultrason. Ferroelectr. Freq. Control*, 2020, doi: 10.1109/TUFFC.2019.2937733.

[60] R. M. Jones, M. A. O'Reilly, and K. Hynynen, "Transcranial passive acoustic mapping with hemispherical sparse arrays using CT-based skull-specific aberration corrections: A simulation study," *Phys. Med. Biol.*, 2013, doi: 10.1088/0031-9155/58/14/4981.

[61] S. Y. Wu *et al.*, "Efficient blood-brain barrier opening in primates with neuronavigation-guided ultrasound and real-time acoustic mapping," *Sci. Rep.*, 2018, doi: 10.1038/s41598-018-25904-9.

[62] A. Y. Ammi, R. O. Cleveland, J. Mamou, G. I. Wang, S. L. Bridal, and W. D. O'Brien, "Ultrasonic contrast agent shell rupture detected by inertial cavitation and rebound signals," *IEEE Trans. Ultrason. Ferroelectr. Freq. Control*, 2006, doi: 10.1109/TUFFC.2006.1588398.